A Parameterized Linear Magnetic Equivalent Circuit for Analysis and Design of Radial Flux Magnetic Gears–Part I: Implementation

Matthew Johnson, *Member, IEEE*, Matthew C. Gardner, *Student Member*, *IEEE*, Hamid A. Toliyat, *Fellow*, *IEEE*

***Abstract*--Magnetic gears offer a promising alternative to mechanical gears with the added benefit of contactless power transfer. However, quick and accurate analysis tools are required to optimize magnetic gear designs and commercialize the technology. Therefore, this work proposes an extremely fast and accurate 2D Magnetic Equivalent Circuit (MEC) model of radial flux magnetic gears with surface mounted magnets. This MEC model's distinguishing characteristics include a heavily parameterized gear geometry and a parametrically adjustable systematic flux tube distribution which allow for accurate and efficient analysis of a wide array of designs. Furthermore, the model is fully linear which results in very quick simulation run times without sacrificing significant torque prediction accuracy for most practical designs. This is Part I of a two part paper and focuses on the implementation of the MEC model. Part II validates the accuracy of the MEC model by comparing its torque and flux density predictions with those produced by nonlinear Finite Element Analysis (FEA).**

***Index Terms*--finite element analysis, magnetic equivalent circuit, magnetic gear, optimization, permeance network, radial flux, reluctance network, torque density.**

I. Introduction

OVER the past two decades, magnetic gears have received significant attention as an intriguing alternative to traditional mechanical gears [1]-[4]. Magnetic gears accomplish the same fundamental behavior as mechanical gears. However, magnetic gears rely on the modulated interaction of fluxes generated by permanent magnets (PMs) on the rotors, instead of mechanical contact between the moving components. This provides a plethora of potential advantages, including inherent overload protection, reduced maintenance requirements, decreased acoustic noise, and physical isolation between the input and output shafts. Thus, magnetically geared systems offer the potential to combine the compact size and cost effectiveness of mechanically geared systems with the reliability of direct drive machines. Additionally, several different magnetically geared machine topologies integrate a magnetic gear directly with a higher speed motor or generator to produce a single extremely compact device capable of directly interfacing with a lower speed, higher torque load or prime mover [5], [6]. Therefore, magnetic gears have received interest for use in a wide variety of applications such as wind turbines [7], wave energy harvesting [8], electric vehicles [6], and electric ships [9].

Nonetheless, magnetic gears still struggle to compete with their mechanical counterparts and achieve parity or superiority with respect to crucial fundamental considerations such as size, weight, and cost [10]. For this technology to realize the full extent of its potential advantages, it is necessary to be able to perform extensive, application specific parametric optimizations [11]. This requires fast and accurate analysis tools capable of characterizing the performance of numerous parametric design variations. The basic tools commonly used for evaluation of electromechanical devices include finite element analysis (FEA) models, analytical models, winding function theory, and magnetic equivalent circuit (MEC) models, all of which can be applied to magnetic gears. While FEA models are generally very accurate, robust, and flexible, analytical and winding function theory models are much faster than FEA but less accurate and less flexible. MEC models represent a compromise between the accuracy and flexibility of FEA models and the speed of analytical models.

The basic concept of an MEC (also known as a reluctance network) is to decompose a physical electromagnetic system into flux tubes (defined paths through which magnetic flux flows) and represent each tube using lumped reluctances, magnetomotive force (MMF) sources, and flux sources to collectively form a lumped parameter magnetic equivalent circuit, which is directly analogous to a traditional lumped parameter electrical circuit and can be solved using the same set of analysis techniques. Just as Kirchhoff's current and voltage laws define the system of equations for an electrical circuit, Gauss's law for magnetism and Ampere's circuital law define the corresponding system of equations for MECs.

Although MEC and FEA models both analyze a system by breaking it up into pieces of varying sizes, there are some

M. Johnson is with the Advanced Electric Machines and Power Electronics Lab in the Department of Electrical and Computer Engineering at Texas A&M University, College Station, TX 77843 USA (e-mail: mjohnson11@tamu.edu).

M. C. Gardner is with the Advanced Electric Machines and Power Electronics Lab in the Department of Electrical and Computer Engineering at Texas A&M University, College Station, TX 77843 USA (e-mail: gardner1100@tamu.edu).

H. A. Toliyat is with the Advanced Electric Machines and Power Electronics Lab in the Department of Electrical and Computer Engineering at Texas A&M University, College Station, TX 77843 USA (e-mail: toliyat@tamu.edu).

critical differences between the two approaches. The most significant distinction is that flux flow directions are predetermined in MEC models by the definition of the flux tubes, but in FEA models the flux orientation in each element is only determined as a result of the model solution. Thus, MEC models typically, although not universally, use scalar quantities such as MMFs (scalar magnetic potentials) or scalar fluxes as the unknown state variables, whereas FEA models commonly use vector quantities, such as vector magnetic potentials. Additionally, MEC models traditionally rely heavily on prior empirical knowledge of system behavior and use significantly fewer elements than FEA models; however, this difference is not necessarily an intrinsic characteristic of the two approaches.

The concepts of a magnetic circuit and reluctance date back well into the 1800s [12]. Furthermore, Hopkinson's Law,

$$\mathcal{F} = \mathcal{R}\Phi \tag{1}$$

was formulated by 1886 and relates the scalar magnetic potential or MMF, $\mathcal{F}$, drop across a flux tube to the magnetic flux, Φ, flowing through the flux tube and the reluctance, $\mathcal{R}$, of the flux tube. Since that time, there have been several studies demonstrating the ability of MEC models to analyze both induction motors and various synchronous machines, often with better accuracy than simplified analytical models and significantly faster simulation run times than corresponding FEA models [13]-[24]. A few works have also established that MEC techniques are well suited for adaptation to 3D models, with their advantages of reduced computational intensity and faster simulation times becoming even more pronounced as compared to 3D FEA models [25]-[27].

This is Part I of a two part study of a generalized, parametric linear MEC model for analysis of the coaxial radial flux magnetic gear topology with surface mounted permanent magnets shown in Fig. 1. The coaxial magnetic gear possesses three rotors: the high speed permanent magnet rotor (HSR), the low speed permanent magnetic rotor (LSR), and the intermediate ferromagnetic modulator rotor. The relationship between the number of permanent magnet pole pairs and the number of modulators is given by

$$Q_M = P_{HS} + P_{LS} \tag{2}$$

where P_{HS} is the number of pole pairs on the HSR, P_{LS} is the number of pole pairs on the LSR, and Q_M is the number of modulators. If the modulators are fixed, the speeds of the HSR and LSR are related by the gear ratio according to

$$\text{Gear Ratio}\big|_{\omega_{Mods}=0} = \frac{\omega_{HS}}{\omega_{LS}} = \frac{-P_{LS}}{P_{HS}} \tag{3}$$

where ω_{HS}, ω_{LS}, and ω_{Mods} are the speeds of the HSR, LSR, and modulators, respectively. Alternatively, if the LSR is fixed and the modulators rotate instead, then the gear ratio becomes positive and increases in magnitude by one to

$$\text{Gear Ratio}\big|_{\omega_{LSR}=0} = \frac{\omega_{HS}}{\omega_{Mods}} = \frac{Q_M}{P_{HS}}. \tag{4}$$

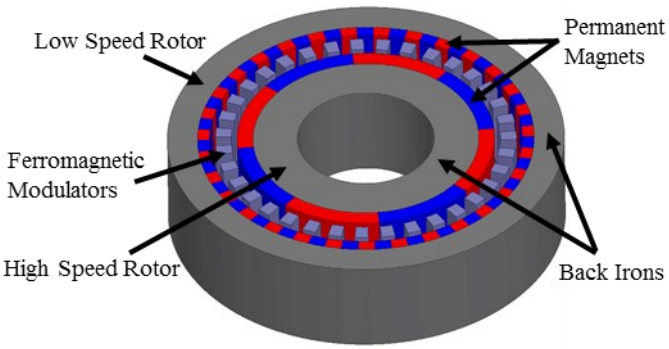

Fig. 1. Radial flux magnetic gear with surface permanent magnets.

Although MECs have been used extensively to model various types of electric machines, there are only a few instances in which the concept has been applied to the analysis of rotary magnetic gears and magnetically geared machines [28]-[31] or linear magnetic gears [32]. Furthermore, while [28]-[31] do demonstrate the potential for MEC models to evaluate a gear design much more rapidly than FEA models, they use extremely coarse reluctance networks with very few elements in the MEC. Also, they provide no analysis of the MEC discretization's impact on its accuracy and little indication of how the MEC's accuracy varies with different design parameters. Additionally, only the work in [30] offers limited discussion of a 3D MEC model with very few elements included to account for axial leakage flux. This study uses an approach more in line with the MEC models developed in [18], [19], [22], and [24]-[27], in the sense that it systematically creates a fully parameterized flux tube mesh by breaking the magnetic gear up into pieces, referred to as node cells. The levels of discretization in different regions of the gear are parameterized so that more mesh elements can be added to the areas that need high resolution for accuracy and fewer elements can be used in the other regions to minimize simulation run times. Finally, whereas [28]-[31] all develop at least partially nonlinear models, this work employs a fully linear MEC model that assumes a constant permeability for both the modulators and the back irons. The evaluation presented in Part II demonstrates that the linear model is still extremely accurate for analysis of the torque capabilities of most reasonable ideal designs, as suggested by the results in [32]. This occurs because the large linear reluctances of the two sets of magnets and the two air gaps dominate the much smaller nonlinear reluctances of the back irons and modulators, even if the back irons and modulators experience significant saturation. The linear model allows for tremendously fast calculation of a gear design's torque capabilities. Furthermore, the MEC implementation, which is described in the following section, is well suited for extension to a nonlinear model using an iterative approach such as the one described in [33]. This extension to a nonlinear model is only necessary for analysis of additional considerations, such as losses or flux densities in the air regions beyond the rotor back irons, or designs which include features, such as a modulator bridge, that significantly increase the system's nonlinearity.

II. The Node Cell

The 2D MEC mesh is systematically formed by dividing the magnetic gear cross-section into radial and circumferential (tangential or angular) layers as illustrated by the simple example shown in Fig. 2, which depicts a source free annular region in the r-θ plane, divided into 3 radial layers (RL) along the r dimension and 8 angular layers (AL) along the θ dimension. Each intersection of a radial layer and an angular layer defines an annular sector, referred to as a 2D node cell. Every 2D node cell consists of two radially directed reluctances and two tangentially directed reluctances, each of which is connected to the center node of the cell and one of the cell's radial or tangential boundaries as shown in Fig. 2. Each of these lumped reluctances corresponds to a flux tube oriented along the same direction, which allows flux to flow in a positive or negative direction along the specified path. In this study, the MEC model is solved using node MMF analysis (which is analogous to node voltage analysis in electrical circuits), based on Gauss's law for magnetism, in which the scalar magnetic potentials at each node represent the unknown state variables. Therefore, it is more appropriate to use lumped permeances rather than their multiplicative inverses, lumped reluctances. An alternate 2D MEC model implementation based on mesh flux analysis techniques derived from Ampere's circuital law was also developed using fluxes as the unknown state variables, but the node MMF approach was ultimately selected for ease of extension to a 3D model, which has already been implemented and will be presented in a future paper. However, while the node potential and mesh flux approaches are essentially computationally equivalent for a linear model, the mesh flux methodology may prove to be computationally advantageous when extending the MEC to a nonlinear model [34].

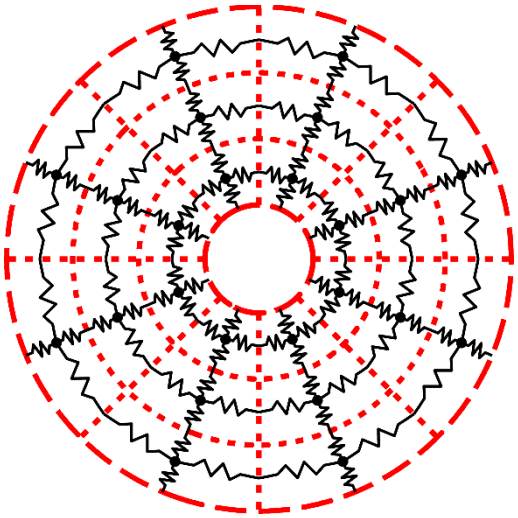

Fig. 2. Definition of mesh node cells based on intersection of radial and angular layers.

The lumped permeance of a uniform flux tube is given by

$$\mathcal{P} = \frac{1}{\mathcal{R}} = \frac{\mu A}{l} \tag{5}$$

where A represents the cross-sectional area of the flux tube surface normal to the flux path, μ is the permeability of the physical material that comprises the flux tube, and l is the total length of the flux tube flux path. Using these relationships, the permeances of each radially directed flux tube ($\mathcal{P}_{rad}$) and each tangentially directed flux tube ($\mathcal{P}_{tan}$) in the reluctance network mesh can be calculated according to the following formulas:

$$\mathcal{P}_{rad} = \left(\int_{r_{in}}^{r_{out}} \frac{dr}{\mu \Delta z (r \Delta\theta)} \right)^{-1} = \frac{\mu \Delta z \Delta\theta}{\ln(r_{out}/r_{in})} \tag{6}$$

$$\mathcal{P}_{tan} = \int_{r_{in}}^{r_{out}} \frac{\mu \Delta z dr}{(\Delta\theta r)} = \left(\frac{\mu \Delta z}{\Delta\theta} \right) \ln\left(\frac{r_{out}}{r_{in}} \right). \tag{7}$$

In each of these equations, r_{in} indicates the inner radius of the flux tube, r_{out} denotes the outer radius of the flux tube, Δθ is the uniform angular width of the flux tube (in radians), Δz is the uniform axial height of the flux tube (which corresponds to the full axial height of the system in a 2D model or the axial height of the axial layer in a 3D model), and μ is the permeability of the flux tube material. If a flux tube overlaps with two different materials, the flux tube is divided into two parts, one for each material region, and the lumped permeances for each part are calculated and then combined in series or parallel, using the same formulas employed for combining series or parallel conductances in electrical circuits.

Conceptual illustrations of radially and tangentially oriented flux tubes are provided in Fig. 3(a) and Fig. 3(b), respectively. Note that each radially directed flux tube corresponds to one radial half of its node cell, the full angular width of its node cell, and the full axial height of its node cell. Equation (6) uses integration to calculate the total lumped radial permeance by combining the reluctances of series connected differential radial slivers of the flux tube. Similarly, each tangentially directed flux tube corresponds to the full radial width of its node cell, one angular half of its node cell, and the full axial height of its node cell. Equation (7) uses integration to combine the permeances of parallel connected differential radial slivers of the flux tube.

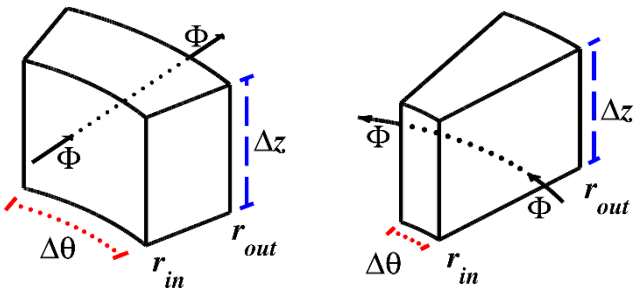

Fig. 3. Conceptual illustrations of (a) radially and (b) tangentially oriented flux tubes.

The appropriate lumped parameter representations of flux tubes corresponding to permanent magnets can be derived by analyzing the linear 2nd quadrant permanent magnet *B-H* curve shown in Fig. 4 and the corresponding linear equation

$$B_{PM} = \mu_{PM} H_{PM} + B_r \tag{8}$$

where B_{PM} and H_{PM} are the magnetic flux density and the magnetic field strength in the permanent magnet, B_r is its remanence or residual flux density, H_c is its coercivity, and μ_{PM} is its recoil permeability defined according to

$$\mu_{PM} = \frac{B_r}{H_c}. \tag{9}$$

Only radially magnetized permanent magnets, and thus only radially oriented flux tubes within permanent magnets are considered in this analysis; however, the same process can easily be extended to permanent magnets with tangential or axial magnetization components for analysis of other magnet configurations such as Halbach arrays or axially oriented systems. Ultimately, the flux tube can be represented by either of the equivalent circuit configurations in Fig 5(a) or Fig 5(b), which are analogous to Thévenin and Norton equivalent circuits, respectively. In both cases, $\mathcal{P}_{rad}$ is the permeance of the radial flux tube assuming a permeability of μ_{PM}. The equivalent MMF and flux injected by the magnet, $\mathcal{F}_{inj}$ and Φ_{inj}, respectively, are given by

$$\mathcal{F}_{inj} = -\frac{B_r}{\mu_{PM}}\left(r_{out} - r_{in}\right) \tag{10}$$

$$\Phi_{inj} = \frac{\mathcal{F}_{inj}}{\mathcal{R}_{rad}}. \tag{11}$$

If a flux tube path overlaps with multiple permanent magnets, then a weighted average of the relevant magnetizations is used to determine the value of the corresponding injected MMF or flux source.

Like the use of Kirchhoff's current law in node voltage analysis of electrical circuits, application of Gauss's law for magnetism to each node cell in the MEC, such as the one shown in Fig. 6, yields a node MMF equation of the form

$$\sum_{i=1}^{4}\left(\mathcal{P}_i \mathcal{F}_x - \mathcal{P}_i \mathcal{F}_i\right) = -\Phi_{inj,2} + \Phi_{inj,4}. \tag{12}$$

For generality, Fig. 6 and (12) describe a permanent magnet node cell; however, the flux source terms are simply set to zero in node cells that do not correspond to permanent magnets. The first term on the left side of (12) is merely the product of the sum of all permeances attached to the target node (node "x") and the MMF of the target node ($\mathcal{F}_x$). This term describes the effect of the target node's MMF on the net flux leaving the node, so it is has a positive permeance coefficient. The second term on the left side of (12) corresponds to each of the nodes adjacent to the target node. Each term in this summation is the product of the permeance connecting the corresponding adjacent node to the target node and the MMF of the adjacent node. These terms all have negative permeance coefficients. The terms on the right side of (12) correspond to the algebraic sum of the injected flux sources flowing into the target node.

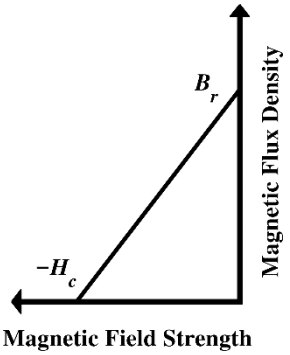

Fig. 4. Linear 2nd quadrant permanent magnet *B-H* curve.

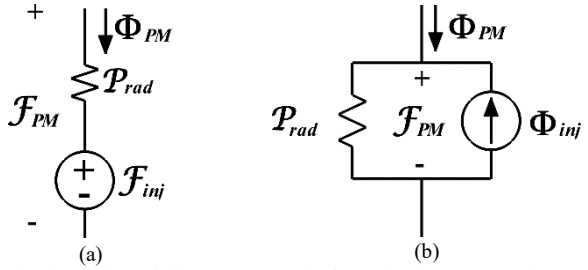

Fig. 5. (a) Thévenin and (b) Norton equivalent circuit representations of radially oriented permanent magnet flux tubes.

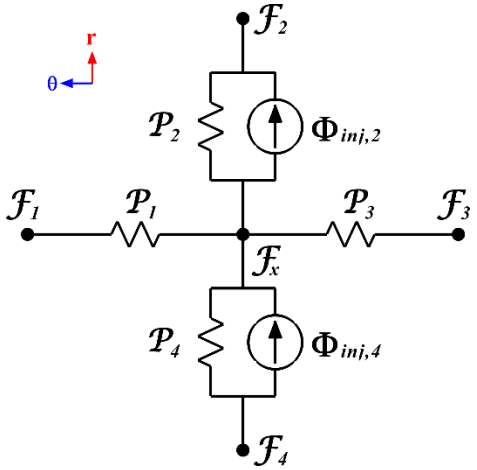

Fig. 6. Annotated 2D node cell schematic.

III. The Permeance Matrix

In light of the analysis of a single 2D node cell, consider the MEC mesh distribution throughout the entire radial flux magnetic gear 2D cross-section. The radial flux magnetic gear geometry shown in Fig. 1 consists of 7 distinct annular radial regions: the HSR back iron, the HSR permanent magnets, the inner HSR air gap, the modulators, the outer LSR air gap, the LSR permanent magnets, and the LSR back iron. Each of these radial regions is meshed according to the previously described methodology depicted in Fig. 2. Each radial region is divided into the same number of angular layers and an independently specified number of radial layers. The number of angular layers used throughout the gear, N_{AL}, and the number of radial layers used in each radial region ($N_{RL,HSBI}$, $N_{RL,HSPM}$, $N_{RL,HSAG}$, $N_{RL,Mods}$, $N_{RL,LSAG}$, $N_{RL,LSPM}$, and $N_{RL,LSBI}$) are 8 independent user controlled parameters that determine the mesh discretization for a 2D MEC model. The lines in Fig. 7 illustrate the flux path network resulting from the application

of a relatively coarse 2D MEC mesh to the full magnetic gear geometry, with N_{AL} = 32, $N_{RL,HSBI}$ = 2, $N_{RL,HSPM}$ = 3, $N_{RL,HSAG}$ = 1, $N_{RL,Mods}$ = 3, $N_{RL,LSAG}$ = 1, $N_{RL,LSPM}$ = 2, and $N_{RL,LSBI}$ = 2. The resulting nodes for this mesh distribution are indicated by the black dots in Fig. 7. Fig. 8 shows an example of the ladder MEC network resulting from an even coarser mesh overlaid on top of an unrolled linear representation of an overly simplistic magnetic gear geometry with P_{HS} = 1, P_{LS} = 2, and Q_M = 3 in the r-θ plane. The left and right edges of Fig. 8 are connected by "wrap around" flux paths (not shown in Fig. 8) in accordance with the circular nature of the actual geometry.

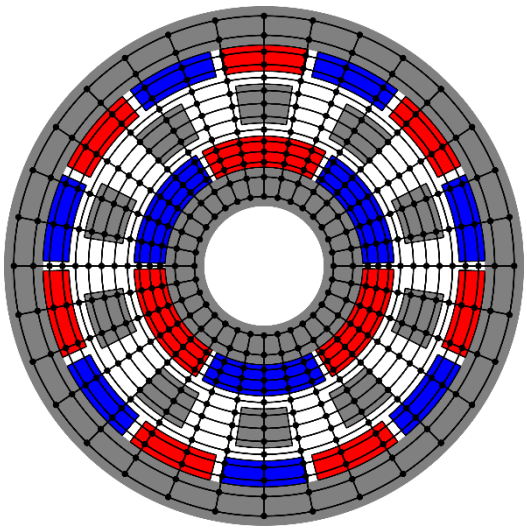

Fig. 7. Example radial flux magnetic gear MEC flux path network.

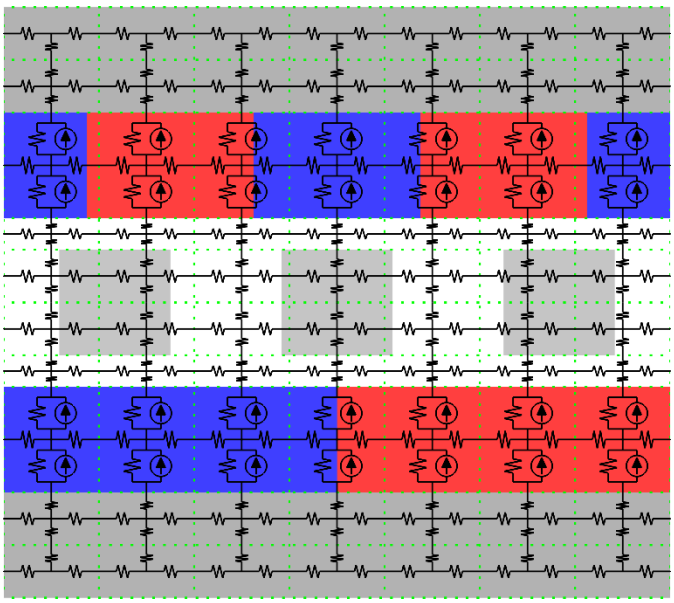

Fig. 8. Example 2D MEC schematic overlay on unrolled radial flux magnetic gear geometry.

Each node in the MEC corresponds to a node MMF equation of the same basic form as the one shown in (12), and there are N_{2D} total nodes in a 2D MEC model, where N_{2D} is the product of the number of angular layers, N_{AL}, and the total number of radial layers, N_{RL}. Thus, the resulting system of linear equations for the full 2D MEC model can be expressed in matrix form according to

$$\mathcal{P}_{2D}\mathcal{F}_{2D} = \Phi_{2D} \tag{13}$$

where $\mathcal{P}_{2D}$ is the (N_{2D} x N_{2D}) 2D system permeance matrix, $\mathcal{F}_{2D}$ is the (N_{2D} x 1) column vector of unknown MMFs for each corresponding node in the 2D MEC, and Φ_{2D} is the (N_{2D} x 1) column vector of the algebraic sums of the injected fluxes from the magnets entering each corresponding node in the 2D MEC. The i^{th} row in $\mathcal{P}_{2D}$ corresponds to the i^{th} node in the MEC and contains the permeance coefficients for that node's MMF equation, such as those shown on the left side of (12). The j^{th} column in $\mathcal{P}_{2D}$ also corresponds to the j^{th} node in the MEC. Entry $\mathcal{P}_{2D(i,j)}$ in $\mathcal{P}_{2D}$ contains the permeance coefficient which describes the impact of the j^{th} node's MMF on the net flux leaving the i^{th} node. Each diagonal entry $\mathcal{P}_{2D(i,i)}$ in $\mathcal{P}_{2D}$ contains the positive sum of all equivalent permeances attached directly to node i. The permeance coefficient of $\mathcal{F}_x$ in (12) is an example of what would become a diagonal entry in the matrix representation of the system of equations. These diagonal entries indicate the impact of the corresponding node's MMF on the net flux leaving that node. Each off-diagonal entry $\mathcal{P}_{2D(i,j)}$ (where $i \neq j$) in $\mathcal{P}_{2D}$ contains the negative value of the equivalent permeance directly connecting nodes i and j. If there is no direct connection between nodes i and j (a permeance path that does not go through another node), then the corresponding entry in $\mathcal{P}_{2D}$ is zero. The permeance coefficients $\mathcal{P}_1$, $\mathcal{P}_2$, $\mathcal{P}_3$, and $\mathcal{P}_4$ in (12) are each examples of what would become off-diagonal entries in the matrix representation of the system of equations.

The overall 2D MEC permeance matrix, $\mathcal{P}_{2D}$, can be constructed in a general form with its constituent submatrices as shown in (14)-(16). The arrangement of these matrices is based on the node numbering system used in the MEC model, in which the first N_{AL} rows and the first N_{AL} columns in $\mathcal{P}_{2D}$ correspond to nodes in the first radial layer, and the next N_{AL} rows and the next N_{AL} columns correspond to nodes in the second radial layer, and so on. The (N_{AL} x N_{AL}) matrix $\mathcal{P}_{RL(k:k)}$ defined in (14) contains the permeance coefficients corresponding to nodes in the k^{th} radial layer. Each diagonal entry $\mathcal{P}_{(k:k),(i:i)}$ in $\mathcal{P}_{RL(k:k)}$ contains the positive sum of all equivalent permeances attached directly to the node at the intersection of the k^{th} radial layer and the i^{th} angular layer. As indicated by (16), the diagonal entries in $\mathcal{P}_{RL(k:k)}$ are also the diagonal entries of $\mathcal{P}_{2D}$. Each off-diagonal entry $\mathcal{P}_{(k:k),(i:j)}$ (where $i \neq j$) in $\mathcal{P}_{RL(k:k),}$ contains the negative value of the equivalent permeance directly connecting the node at the intersection of the k^{th} radial layer and the i^{th} angular layer and the node at the intersection of the k^{th} radial layer and the j^{th} angular layer. Because all permeances in the MEC are bidirectional, each matrix $\mathcal{P}_{RL(k:k)}$ is symmetric.

$$\mathcal{P}_{RL(k:k)} = \begin{bmatrix} \mathcal{P}_{(k:k),(1:1)} & -\mathcal{P}_{(k:k),(1:2)} & 0 & \cdots & 0 & -\mathcal{P}_{(k:k),(1:N_{AL})} \\ -\mathcal{P}_{(k:k),(2:1)} & \mathcal{P}_{(k:k),(2:2)} & -\mathcal{P}_{(k:k),(2:3)} & 0 & \cdots & 0 \\ 0 & -\mathcal{P}_{(k:k),(3:2)} & \ddots & \ddots & \ddots & \vdots \\ \vdots & 0 & \ddots & \ddots & \ddots & 0 \\ 0 & \vdots & \ddots & \ddots & \ddots & -\mathcal{P}_{(k:k),(N_{AL}-1:N_{AL})} \\ -\mathcal{P}_{(k:k),(N_{AL}:1)} & 0 & \cdots & 0 & -\mathcal{P}_{(k:k),(N_{AL}:N_{AL}-1)} & \mathcal{P}_{(k:k),(N_{AL}:N_{AL})} \end{bmatrix} \tag{14}$$

$$\mathcal{P}_{RL(k:k-1)} = \mathcal{P}_{RL(k-1:k)} = \begin{bmatrix} \mathcal{P}_{(k:k-1),(1:1)} & 0 & \cdots & 0 \\ 0 & \mathcal{P}_{(k:k-1),(2:2)} & \ddots & \vdots \\ \vdots & \ddots & \ddots & 0 \\ 0 & \cdots & 0 & \mathcal{P}_{(k:k-1),(N_{AL}:N_{AL})} \end{bmatrix} \tag{15}$$

$$\mathcal{P}_{2D} = \begin{bmatrix} \mathcal{P}_{RL(1:1)} & -\mathcal{P}_{RL(1:2)} & 0 & \cdots & 0 \\ -\mathcal{P}_{RL(2:1)} & \mathcal{P}_{RL(2:2)} & -\mathcal{P}_{RL(2:3)} & \ddots & \vdots \\ 0 & -\mathcal{P}_{RL(3:2)} & \ddots & \ddots & 0 \\ \vdots & \ddots & \ddots & \ddots & -\mathcal{P}_{RL(N_{RL}-1:N_{RL})} \\ 0 & \cdots & 0 & -\mathcal{P}_{RL(N_{RL}:N_{RL}-1)} & \mathcal{P}_{RL(N_{RL}:N_{RL})} \end{bmatrix} \tag{16}$$

The (N_{AL} x N_{AL}) matrix $\mathcal{P}_{RL(k:k-1)}$ defined in (15) contains the permeances corresponding to paths directly connecting nodes in the k^{th} radial layer to adjacent nodes in radial layer k-1. Each diagonal entry $\mathcal{P}_{(k:k-1),(i:i)}$ in $\mathcal{P}_{RL(k:k-1)}$ contains the equivalent permeance directly connecting the i^{th} node in the k^{th} radial layer to the i^{th} node in radial layer k-1. All other entries in $\mathcal{P}_{RL(k:k-1)}$ are zero. Because all permeances in the MEC are bidirectional, the matrix $\mathcal{P}_{RL(k-1:k)}$ is always equal to $\mathcal{P}_{RL(k:k-1)}$. $\mathcal{P}_{2D}$, is then constructed from these constituent submatrices, as shown in (16). Thus, the matrix $\mathcal{P}_{2D}$ is always symmetric.

Each node in the 2D MEC has four adjacent nodes: one on each of the radial inside, the radial outside, the clockwise circumferential side, and the counterclockwise circumferential side. The only exceptions are the nodes in the innermost and outermost radial layers, which do not have any adjacent nodes on the radial inside and radial outside, respectively. Consequently, each row in $\mathcal{P}_{2D}$ corresponding to a node in the first or last radial layers has four non-zero entries, and all other rows have five non-zero entries, one for each adjacent node, as well as the diagonal entry in each row. Thus, N_{NZ2D}, the total number of non-zero entries in $\mathcal{P}_{2D}$, is given by

$$N_{NZ2D} = N_{AL}\left(5N_{RL} - 2\right) \tag{17}$$

and the sparsity of $\mathcal{P}_{2D}$ can be calculated according to

$$\text{Sparsity of } \mathcal{P}_{2D} = \left(1 - \frac{N_{NZ2D}}{N_{2D}^2}\right)100\%\,. \tag{18}$$

Consequently, permeance matrices resulting from MEC models with reasonable mesh resolutions are extremely sparse; therefore, the MATLAB implementation of the MEC model stores $\mathcal{P}_{2D}$ as a sparse matrix in order to dramatically reduce the amount of memory used by the program. For example, for each of the three base designs used in Part II, $\mathcal{P}_{2D}$ has a sparsity of at least 99.96% for both the fine and coarse mesh settings.

IV. Solving the System

The 2D MEC model is solved by solving the linear system of equations given in (13) for the N_{2D} unknown node MMFs in

the column vector $\mathcal{F}_{2D}$. If the 2D MEC model has symmetry, then it can be analyzed by solving only the subset of equations corresponding to nodes in a symmetrical fraction of the model. Because MMF values represent scalar potentials with respect to a reference node, in full 2D MEC models or fractional models with even symmetry, the first node is defined as the zero potential reference for the rest of the system. This allows the first row of $\mathcal{P}_{2D}$ and Φ_{2D} and the first column of $\mathcal{P}_{2D}$ to be eliminated, and the remaining system can be solved. However, for models with odd symmetry, it is desirable for corresponding nodes in adjacent fractions of the model to have potentials with the same magnitudes and opposite signs. This choice effectively determines the zero potential reference, which may not correspond to any of the nodes. Thus, for models with odd symmetry, the first row of $\mathcal{P}_{2D}$ and Φ_{2D} and the first column of $\mathcal{P}_{2D}$ must not be eliminated.

In theory, the solution to the system can be obtained by inverting the relevant portion of the permeance matrix, based on the application of the preceding discussion of symmetry and the reference node. However, most practical MEC models with adequate mesh resolution result in system permeance matrices which would require a relatively significant amount of time and memory to invert; therefore, this implementation solves the MEC system by factorizing the matrix and solving the corresponding triangular systems as described in [35]. This approach dramatically decreases the amount of memory and simulation time required to solve an MEC model. To evaluate the design at different rotor positions, it is necessary to repeat this process with an adjusted permeance matrix and injected flux vector. However, if the recoil permeability of the magnets is approximated as the permeability of free space (or if the magnets have a 100% tangential fill factor) and the modulators are used as the reference frame, only the injected flux vector must be adjusted. This can result in significant time savings because the permeance matrix only needs to be factorized once per design, regardless of the rotor orientations.

Once an MEC model has been solved for the vector of node MMFs, this information can be used along with the reluctances of the flux tubes to calculate various other quantities of interest, such as the flux in any flux tube and the flux density at any position in the gear. Due to their coarse flux tube distributions, many of the other MEC models described in the literature, including most of the few previous magnetic gear MEC studies [28]-[30], [32], use the virtual work (coenergy) method to calculate torque. However, this implementation uses Maxwell stress tensors for torque calculations from the more detailed solutions provided by its higher resolution flux tube distributions. In particular, the torque on the HSR, τ_{HSR}, and the torque on the LSR, τ_{LSR}, are calculated using Maxwell stress tensors according to

$$\tau_{HSR} = \left(\frac{r_{HS}^2}{\mu_0}\right)\left(\frac{2\pi}{N_{AL}}\right)\sum_{i=1}^{N_{AL}} B_r\left(r_{HS},i\right)B_\theta\left(r_{HS},i\right) \qquad (19)$$

$$\tau_{LSR} = -\left(\frac{r_{LS}^2}{\mu_0}\right)\left(\frac{2\pi}{N_{AL}}\right)\sum_{i=1}^{N_{AL}} B_r\left(r_{LS},i\right)B_\theta\left(r_{LS},i\right). \qquad (20)$$

where r_{HS} and r_{LS} represent the radii of the integration (summation) paths in the high and low speed air gaps, while $B_r(r,i)$ and $B_\theta(r,i)$ represent the radial and tangential components of the magnetic flux density in the i^{th} angular layer at the specified radius. This study uses integration paths corresponding to the radial middle of node cells in the middle layer of each air gap. The flux densities are linearly interpolated with respect to radius and are assumed to be invariant with respect to angle within a flux tube. The torque on the entire modulator structure, τ_{Mods}, is then given by

$$\tau_{Mods} = -\left(\tau_{HSR} + \tau_{LSR}\right). \qquad (21)$$

V. Conclusions

This is the first part of a two part paper on the development of a radial flux magnetic gear MEC model. This part presents the systematic implementation of the MEC model, while Part II provides a thorough evaluation and validation of the model's accuracy by comparing its torque and flux density predictions against those produced by a commercial non-linear FEA model. The MEC model is constructed by dividing the magnetic gear into radial and angular layers. The number of radial layers in each of the magnetic gear's 7 different radial regions and the number of angular layers are all independently controlled by 8 user specified resolution parameters. Each annular sector defined by the intersection of a radial layer and an angular layer corresponds to a node cell, which is the basic building block of the MEC. The center of each node cell is a node in the magnetic equivalent circuit. Every node cell also contains two radially directed reluctances and two tangentially directed reluctances, which connect the node to the cell's boundaries. The reluctances in any one node cell connect to reluctances in neighboring cells and link all of the nodes together to form the MEC system network.

The (N_{2D} x N_{2D}) MEC system permeance matrix defined in (16) contains one row and one column for each node in the network. This matrix defines the relationship between each of the N_{2D} node MMFs in the MEC, as described by the system matrix equation given in (13), and it is formed based on the user specified discretization settings, magnetic gear geometrical design parameters, and material properties. Because the system permeance matrix is constructed using user specified fixed permeabilities for the different materials, the MEC model and system of equations are linear. Once the permeance matrix is constructed, it is factorized to solve the system of equations and calculate the MMF of each node in the MEC. This particular implementation capitalizes on any symmetry in the gear geometry, as well as the symmetry and sparsity of the permeance matrix to accelerate the solution process and reduce its memory requirements. The node MMFs can then be used along with the discrete MEC permeances to solve for flux densities and other quantities of interest, such as the torques on the different gear subsystem bodies. This systematic implementation of a linear MEC model allows for extremely fast and accurate analysis of a wide range of practical magnetic gear designs, as demonstrated by the various results provided in Part II.

VI. References

[1] K. Atallah and D. Howe, "A Novel High-Performance Magnetic Gear," *IEEE Trans. Magn.,* vol. 37, no. 4, pp. 2844-2846, Jul. 2001.

[2] N. W. Frank and H. A. Toliyat, "Analysis of the Concentric Planetary Magnetic Gear with Strengthened Stator and Interior Permanent Magnet Inner Rotor," *IEEE Trans. Ind. Appl.,* vol. 47, no. 4, pp. 1652-1660, Jul.-Aug. 2011.

[3] P. O. Rasmussen, T. O. Andersen, F. T. Jorgensen, and O. Nielsen, "Development of a High-Performance Magnetic Gear," *IEEE Trans. Ind. Appl.,* vol. 41, no. 3, pp. 764-770, May-Jun. 2005.

[4] P. M. Tlali, R.-J. Wang, and S. Gerber, "Magnetic Gear Technologies: A Review," in *Proc. Int. Conf. Elect. Mach.*, 2014, pp. 544-550.

[5] M. Johnson, M. C. Gardner, and H. A. Toliyat, "Design and Analysis of an Axial Flux Magnetically Geared Generator," *IEEE Trans. Ind. Appl.,* vol. 53, no. 1, pp. 97-105, Jan.-Feb. 2017.

[6] T. V. Frandsen, L. Mathe, N. I. Berg, R. K. Holm, T. N. Matzen, P. O. Rasmussen, and K. K. Jensen, "Motor Integrated Permanent Magnet Gear in a Battery Electrical Vehicle," *IEEE Trans. Ind. Appl.,* vol. 51, no. 2, pp. 1516-1525, Mar.-Apr. 2015.

[7] N. W. Frank and H. A. Toliyat, "Gearing Ratios of a Magnetic Gear for Wind Turbines," in *Proc. IEEE Int. Elect. Mach. and Drives Conf.*, 2009, pp. 1224-1230.

[8] K. K. Uppalapati, J. Z. Bird, D. Jia, J. Garner, and A. Zhou, "Performance of a Magnetic Gear Using Ferrite Magnets for Low Speed Ocean Power Generation," in *Proc. IEEE Energy Convers. Congr. and Expo.*, 2012, pp. 3348-3355.

[9] N. W. Frank and H. A. Toliyat, "Gearing Ratios of a Magnetic Gear for Marine Applications," in *Proc. IEEE Electr. Ship Technol. Symp.*, 2009, pp. 477-481.

[10] E. Gouda, S. Mezani, L. Baghli, and A. Rezzoug, "Comparative Study between Mechanical and Magnetic Planetary Gears," *IEEE Trans. Magn.,* vol. 47, no. 2, pp. 439-450, Feb. 2011.

[11] M. Johnson, M. C. Gardner, and H. A. Toliyat, "Design Comparison of NdFeB and Ferrite Radial Flux Magnetic Gears," in *Proc. IEEE Energy Convers. Congr. and Expo.*, 2016, pp. 1-8.

[12] J. F. H. Douglas, "The Reluctance of Some Irregular Magnetic Fields," *Trans. AIEE,* vol. XXXIV, no. 1, pp. 1067-1134, Apr. 1915.

[13] E. R. Lwithwaite, "Magnetic Equivalent Circuits for Electrical Machines," *Proc. Inst. Electr. Eng.,* vol. 114, no. 11, pp. 1805-1809, Nov. 1967.

[14] C. J. Carpenter, "Magnetic Equivalent Circuits," *Proc. Inst. Electr. Eng.,* vol. 115, no. 10, pp. 1503-1511, Oct. 1968.

[15] V. Ostovic, "A Method for Evaluation of Transient and Steady State Performance in Saturated Squirrel Cage Induction Machines," *IEEE Trans. Energy Convers.,* vol. EC-1, no. 3, pp. 190-197, Sept. 1986.

[16] V. Ostovic, "Computation of Saturated Permanent-Magnet AC Motor Performance by Means of Magnetic Circuits," *IEEE Trans. Ind. Appl.,* vol. IA-23, no. 5, pp. 836-841, Sept. 1987.

[17] V. Ostovic, "A Novel Method for Evaluation of Transient States in Saturated Electric Machines," *IEEE Trans. Ind. Appl.,* vol. 25, no. 1, pp. 96-100, Jan.-Feb. 1989.

[18] C. B. Rasmussen and E. Ritchie, "A Magnetic Equivalent Circuit Approach for Predicting PM Motor Performance," in *Conf. Rec. IEEE Ind. Appl. Soc. Annu. Meeting*, 1997, pp. 10-17 vol.1.

[19] J. Perho, "Reluctance Network for Analysing Induction Machines," Ph.D. dissertation, Dept. Elect. and Commun. Eng., Helsinki Univ. Tech., Espoo, Finland, 2002.

[20] S. D. Sudhoff, B. T. Kuhn, K. A. Corzine, and B. T. Branecky, "Magnetic Equivalent Circuit Modeling of Induction Motors," *IEEE Trans. Energy Convers.,* vol. 22, no. 2, pp. 259-270, Jun. 2007.

[21] M. Yilmaz and P. T. Krein, "Capabilities of Finite Element Analysis and Magnetic Equivalent Circuits for Electrical Machine Analysis and Design," in *Proc. IEEE Power Electron. Specialists Conf.*, 2008, pp. 4027-4033.

[22] M. Amrhein and P. T. Krein, "Magnetic Equivalent Circuit Simulations of Electrical Machines for Design Purposes," in *Proc. IEEE Elect. Ship Technol. Symp.*, 2007, pp. 254-260.

[23] M. F. Hsieh and Y. C. Hsu, "A Generalized Magnetic Circuit Modeling Approach for Design of Surface Permanent-Magnet Machines," *IEEE Trans. Ind. Electron.,* vol. 59, no. 2, pp. 779-792, Feb. 2012.

[24] C. Bruzzese, D. Zito, and A. Tessarolo, "Finite Reluctance Approach: A Systematic Method for the Construction of Magnetic Network-Based Dynamic Models of Electrical Machines," in *Proc. AEIT Annu. Conf.*, 2014, pp. 1-6.

[25] M. Amrhein and P. T. Krein, "Magnetic Equivalent Circuit Modeling of Induction Machines Design-Oriented Approach with Extension to 3-D," in *Proc. IEEE Int. Elect. Mach. and Drives Conf.*, 2007, pp. 1557-1563.

[26] M. Amrhein and P. T. Krein, "3-D Magnetic Equivalent Circuit Framework for Modeling Electromechanical Devices," *IEEE Trans. Energy Convers.,* vol. 24, no. 2, pp. 397-405, Jun. 2009.

[27] M. Amrhein and P. T. Krein, "Force Calculation in 3-D Magnetic Equivalent Circuit Networks with a Maxwell Stress Tensor," *IEEE Trans. Energy Convers.,* vol. 24, no. 3, pp. 587-593, Sept. 2009.

[28] M. Fukuoka, K. Nakamura, and O. Ichinokura, "Dynamic Analysis of Planetary-Type Magnetic Gear Based on Reluctance Network Analysis," *IEEE Trans. Magn.,* vol. 47, no. 10, pp. 2414-2417, Oct. 2011.

[29] M. Fukuoka, K. Nakamura, and O. Ichinokura, "A Method for Optimizing the Design of SPM Type Magnetic Gear Based on Reluctance Network Analysis," in *Proc. Int. Conf. Elect. Mach.*, 2012, pp. 30-35.

[30] D. Thyroff, S. Meier, and I. Hahn, "Modeling Integrated Magnetic Gears Using a Magnetic Equivalent Circuit," in *Proc. Annu. Conf. IEEE Ind. Electron. Soc.*, 2015, pp. 2904-2908.

[31] R. Benlamine, T. Hamiti, F. Vangraefschepe, F. Dubas, and D. Lhotellier, "Modeling of a Coaxial Magnetic Gear Equipped with Surface Mounted PMs Using Nonlinear Adaptive Magnetic Equivalent Circuits," in *Proc. Int. Conf. Elect. Mach.*, 2016, pp. 1888-1894.

[32] R. C. Holehouse, K. Atallah, and J. Wang, "A Linear Magnetic Gear," in *Proc. Int. Conf. Elect. Mach.*, 2012, pp. 563-569.

[33] M. F. Hsieh and Y. C. Hsu, "A Generalized Magnetic Circuit Modeling Approach for Design of Surface Permanent-Magnet Machines," *IEEE Trans. Ind. Electron.,* vol. 59, no. 2, pp. 779-792, Feb. 2012.

[34] H. W. Derbas, J. M. Williams, A. C. Koenig, and S. D. Pekarek, "A Comparison of Nodal- and Mesh-Based Magnetic Equivalent Circuit Models," *IEEE Trans. Energy Convers.,* vol. 24, no. 2, pp. 388-396, Jun. 2009.

[35] T. A. Davis, "Algorithm 930: FACTORIZE: An Object-Oriented Linear System Solver for MATLAB," *ACM Trans. Math. Softw.,* vol. 39, no. 4, pp. 1-18, Jul. 2013.

VII. Biographies

Matthew Johnson (S' 13, M'17) earned his B.S. in electrical engineering with a minor in mathematics from Texas A&M University, College Station, Texas in 2011. In 2017, he received a Ph.D. in electrical engineering while working in the Advanced Electric Machines and Power Electronics Laboratory at Texas A&M University. His research interests include magnetic gears, magnetically geared machines, and motor drives.

Matthew C. Gardner (S' 15) earned his B.S. in electrical engineering with a minor in Computer Science from Baylor University, Waco, Texas in 2014. He is currently pursuing a Ph.D. in electrical engineering while working in the Advanced Electric Machines and Power Electronics Laboratory at Texas A&M University. His research interests include optimal design and control of magnetic gears and magnetically geared machines.

Hamid A. Toliyat (S'87, M'91, SM'96, F'08) received the B.S, degree from Sharif University of Technology, Tehran, Iran in 1982, the M.S. degree from West Virginia University, Morgantown, WV in 1986, and the Ph.D. degree from University of Wisconsin-Madison, Madison, WI in 1991, all in electrical engineering. Following receipt of the Ph.D. degree, he joined the faculty of Ferdowsi University of Mashhad, Mashhad, Iran as an Assistant Professor of Electrical Engineering. In March 1994 he joined the Department of Electrical and Computer Engineering, Texas A&M University where he is currently the Raytheon endowed professor of electrical engineering. Dr. Toliyat has many papers and awards to his name, including the Nikola Tesla Field Award.